Supporting Information for "Global structure of magnetotail reconnection revealed by mining space magnetometer data"

G. K. Stephens[1], M. I. Sitnov[1], R. S. Weigel[2], D. L. Turner[1], N. A. Tsyganenko[3], A. J. Rogers[4], K. Genestreti[5], and J. A. Slavin[6]

[1]The Johns Hopkins University Applied Physics Laboratory, Laurel, MD 20723, USA

[2]George Mason University, Fairfax, VA 22030, USA

[3]Saint-Petersburg State University, Saint-Petersburg, Russia

[4]University of New Hampshire, Durham, NH, USA

[5]Space Science and Engineering, Southwest Research Institute, Durham, NH, USA

[6]Department of Climate and Space Sciences and Engineering, University of Michigan, Ann Arbor, MI, USA

Contents of this file

1. Supporting Information Text

2. Figures S1 to S15

3. Tables S1 to S2

Supporting Information Text

Space Magnetometer Data

The heritage of the space magnetometer data used in this study dates to earlier data mining (DM) reconstructions of storms (Sitnov et al., 2008). As this DM approach relies on knowledge of the solar wind plasma and IMF conditions, the start of the magnetometer archive (January 1995) was chosen to approximately coincide with the advent of continuous long-term L1 monitoring of the upstream solar wind which began in late 1994 with the launch of the Wind spacecraft. That archive (N. A. Tsyganenko & Sitnov, 2007) consisted of magnetic field observations from the IMP-8, Geotail, the Geosynchronous GOES-8, 9, 10, and 12 satellites, Cluster, and Polar missions. The time-resolution of the magnetometer data provided by the missions is often higher than is necessary for global scale reconstructions so it is common practice to downsample the original data source to a regular cadence by time-averaging over multiple measurements, e.g., (N. Tsyganenko et al., 2021). A decision must then be made for the frequency of the downsampled data. The archive from (N. A. Tsyganenko & Sitnov, 2007; Sitnov et al., 2008) choose 15 min averaging cadence except for when spacecraft were located within $r < 5R_E$, in which the higher spacecraft velocities prompted for a 5 min data cadence. This archive is available at http://geo.phys.spbu.ru/∼tsyganenko/data_sets.html.

The data archive from (N. A. Tsyganenko & Sitnov, 2007) was later augmented for the DM reconstructions of substorms by updating the Polar and Cluster datasets and by adding the THEMIS and Van Allen probes magnetometer data (Stephens et al., 2019). This expansion proved useful in populating the equatorial inner magnetosphere and near-

tail region with data. In constructing this archive, the data from these four missions was averaged to a 5 min cadence, but when incorporated into the DM algorithm, it was downsampled to 15 min when the spacecraft location was $r \geq 5R_E$ to be consistent with the earlier archive. This database is available on the NASA Space Physics Data Facility: https://spdf.sci.gsfc.nasa.gov/pub/data/aaa_special-purpose-datasets/empirical-magnetic-field-modeling-database-with-TS07D-coefficients/. This was again extended in subsequent substorm reconstructions by adding the available MMS data, which at that time had completed a full season sampling the midtail following the extension of the MMS apogee to $r \approx 25R_E$ (Sitnov et al., 2019; Stephens & Sitnov, 2021). The addition of MMS data proved useful in the reconstruction of the mid-tail region including the resolution of X-line features (Sitnov et al., 2019). For these substorm reconstructions, data beyond the primary apogee of the Geotail mission, $r = 31R_E$, was filtered. This was performed primarily to remove data points from the two THEMIS probes as they transitioned to the ARTEMIS orbit, as the inclusion of this distant data could produce anomalous results (Stephens et al., 2019).

In this study, the magnetometer data archive has again been updated. Fist, given the importance of the MMS dataset to this particular investigation, it was extended through the end of the year 2020, now encompassing three full tail seasons. Further, in February of 2019, the MMS apogee was raised from $r \approx 25R_E$ to $r \approx 29R_E$ (Williams et al., 2020), increasing the amount of data in this region. Second, the THEMIS, Cluster, Van Allen Probes, and MMS datasets were all downsampled to a universal 5 min cadence, instead of switching between 5 and 15 min based on spacecraft's radial distance. The

motivation being that the previous substorm investigations demonstrated that the DM approach can indeed reconstruct changes in the magnetosphere on the scale approaching 5 min resolution (Stephens et al., 2019; Sitnov et al., 2019). Further, this makes the cadence of the magnetometer archive consistent with that of the model reconstructions and the OMNI dataset. The remaining spacecraft datasets (Geotail, IMP-8, and GOES satellites) retain the 15 min data cadence only because upgrading them would require additional efforts beyond the scope of this study. The third is that the radial filter was increased from $31R_E$ to $36R_E$. Although, as Fig. S1 indicates, the data between $31R_E$ and $36R_E$ is relatively sparse, its inclusion was found to help stabilize the reconstructions in the region $r \approx 25$–$31R_E$, which was of particular importance for this study. The result is an archive of 8,649,672 magnetometer data records spanning the years 1995–2020 and radial distance 1.5 to $36R_E$. The resulting spatial distribution of the archive is shown in Fig. S1 while the breakdown of each individual spacecraft's contribution to the archive is displayed in Table S1.

The general process for constructing these datasets is as follows. First, the magnetometer data is downloaded from either the mission webpage or a community resource such as the NASA Space Physics Data Facility. Any anomalous data records are removed. The contribution of the internal magnetic field is removed utilizing the International Geomagnetic Reference Field (Alken et al., 2021) (IGRF model). Data collected when the spacecraft was outside the magnetopause is filtered by either visual determination of magnetopause crossings or by application of empirical magnetopause models, e.g., (Shue et al., 1998). The resulting data are then downsampled to the requisite data cadence using

boxcar averaging. As one approaches the surface of the Earth, the value of the background magnetic field, B_{int}, becomes very large relative to the magnetic field generated by external current sources, B_{ext}. Thus, distinguishing the external and internal fields requires attitude knowledge beyond the capacity of many spacecraft missions. For these reasons data is excluded when $r < 1.5R_E$ for equatorial orbiting spacecraft. For polar orbiting spacecraft (Polar and Cluster), a larger exclusion radius of $r < 3.2R_E$ was used to prevent the large magnetic field deviations due to low-altitude FACs from biasing the fit.

Storm-Substorm-Solar Wind State-Space

Storms and substorms and their response to solar wind drivers have a tendency to develop in repeatable and predictable ways as indicated by their manifestation in geomagnetic indices, e.g., (Liemohn et al., 2018). This makes their empirical reconstruction using DM possible. To do this, the storm/substorm state of the magnetosphere is assumed to be characterizable using a low-dimensional state-space (Vassiliadis, 2006). For example, earlier storm studies formulated a 3D state-space based on the storm-time index *Sym-H*, its time derivative, and the solar wind electric field parameter vB_z^{IMF} (Sitnov et al., 2008) (where v is the X component of the solar wind bulk velocity which is multiplied by the Z component of the IMF in GSM coordinates), the idea being that these three parameters are representative of the storm state of the magnetosphere (Burton et al., 1975; Vassiliadis et al., 1999). At any given moment in time the storm-state of the magnetosphere is represented as a state-vector, $\mathbf{G}(t)$, within this state-space. As the storm develops, it will plot a trajectory through this state-space and similar events will trace

similar trajectories. Subsequent substorm investigations expanded to a 5D state-space by adding the substorm index AL along with its time derivative (Stephens et al., 2019). For this study, the AL and *Sym-H* indices have been replaced by their SuperMAG counterparts (Gjerloev, 2012), SML and SMR respectively (Newell & Gjerloev, 2011, 2012). The primary reason for this change was that, as of the writing of this study, the digital values for the AL index are not available beyond March of 2018. This would have nullified the expansion of the MMS dataset discussed in the previous section. Further, although not officially authorized by the International Association of Geomagnetism and Aeronomy, the SuperMAG indices are computed using a much higher number of ground magnetometer stations (on the order of ~ 100 instead of ~ 10). In particular, the higher density and smaller gaps between stations allows the SML index to detect substorms that may be missed by the AL index (Newell & Gjerloev, 2011). As with the earlier studies, the storm index has been pressure corrected to remove magnetic perturbations caused by the compression of the magnetopause (Gonzalez et al., 1994). The pressure corrected index, $SMRc$, is defined: $SMRc = 0.8 \cdot SMR - 13\sqrt{P_{dyn}}$ (N. A. Tsyganenko et al., 2021). The 5D storm/substorm state-space used here is defined:

$$G_1^{(sst)}(t) = \langle SMRc| \propto \int_{-\Pi_{st}/2}^{0} SMRc(t+\tau)\cos\left(\pi\tau/\Pi_{st}\right)\mathrm{d}\tau \tag{1}$$

$$G_2^{(sst)}(t) = \mathrm{D}\langle SMRc|/\mathrm{D}t \propto \int_{-\Pi_{st}/2}^{0} SMRc(t+\tau)\cos\left(2\pi\tau/\Pi_{st}\right)\mathrm{d}\tau \tag{2}$$

$$G_3^{(sst)}(t) = \langle SML| \propto \int_{-\Pi_{sst}/2}^{0} SML(t+\tau)\cos\left(\pi\tau/\Pi_{sst}\right)\mathrm{d}\tau \tag{3}$$

$$G_4^{(sst)}(t) = \mathrm{D}\langle SML|/\mathrm{D}t \propto \int_{-\Pi_{sst}/2}^{0} SML(t+\tau)\cos\left(2\pi\tau/\Pi_{sst}\right)\mathrm{d}\tau \tag{4}$$

$$G_5^{(sst)}(t) = \langle vB_s^{IMF}| \propto \int_{0}^{\tau_\infty} vB_s^{IMF}(t-\tau_\infty+\tau)\exp\left[(\tau-\tau_\infty)/\tau_0\right]\mathrm{d}\tau \tag{5}$$

The integration convolves the original time-series data with smoothing windows. In the case of eq. (1) and eq. (3) the windows are half cosines which acts to smooth *SMRc* and *SML* over storm ($\Pi_{st}/2 = 6$ h) and substorms scales ($\Pi_{sst}/2 = 1$ h) respectively (Stephens et al., 2019). Meanwhile, their smoothed time derivatives, eq. (2) and eq. (4), are defined using two half cosine masks as described in (Sitnov et al., 2012). The fifth parameter, eq. (5), uses an exponential function to smooth over vB_s^{IMF} (where $B_s^{IMF} = -B_z^{IMF}$ when $B_z^{IMF} < 0$ and $B_s^{IMF} = 0$ otherwise). The exponential function not only acts as a smoothing window but also captures the loading of magnetic flux in the lobes during the substorm growth phase, thus, the e-folding time, $\tau_0 = 0.5$ h, was set based on the typical duration of the growth phase (Partamies et al., 2013). Six e-foldings were used in the convolution, $\tau_\infty = 6\tau_0$. Note, the integration only occurs over past data, as indicated by the limits of integration in eqs. (1)–(5), to prevent non-casual effects, that is, to prevent **G** from reacting to changes that have not yet occurred. The scale of each dimension of the state-space is standardized by dividing the above equations by their standard deviation

(computed over the entirety of the state-space), as is indicated by the proportionality signs.

The solar wind plasma and IMF measurements were obtained from the NASA Space Physics Data Facility through OMNIWeb (https://omniweb.gsfc.nasa.gov/ow_min.html). OMNIWeb utilizes solar wind measurements from the ACE, Wind, IMP 8, and Geotail mission's magnetic field and plasma instruments applying a time delay to propagate them to the bow shock nose. The 5-min cadence OMNI products were used throughout this study, including the values for the solar wind velocity, flow pressure, and the IMF. The *SML* and *SMR* 1-min indices were downloaded through the SuperMAG webpage (https://supermag.jhuapl.edu/indices).

Mining Data Using k-Nearest Neighbors

Our approach resembles the k-Nearest Neighbor (kNN) method of data mining (DM) (Vassiliadis et al., 1995; Wettschereck et al., 1997), but also has important distinctions (Sitnov et al., 2008; Stephens et al., 2019). First, while the kNN subsets are first identified in the state-space, the magnetic field reconstruction is performed in the real space using magnetometer observations that occurred during those k_{NN} moments. The choice of the number of k_{NN} must be ample enough to fit flexible magnetic field models with high degrees of freedom (N. A. Tsyganenko & Sitnov, 2007; Stephens et al., 2019) while at the same time sufficiently small, $1 \ll k_{NN} \ll k_{SS}$ where k_{SS} is the number of points in the whole state-space, as to provide adequate sensitivity to the storm and substorm phases. Second, the state-space includes the smoothed time derivatives of the activity

indices to increase the sensitivity of the DM procedure to these phases and to capture memory effects of the magnetosphere as a dynamic system (Sitnov et al., 2001).

In the DM method the state and input variables eqs. (1)–(5) are used to define the distance $R_q^{(i)} < R_{NN}$ of k_{NN} nearest neighbors from the query point $G_k^{(q)}$ $(k = 1, ..., 5)$:

$$R_q^{(i)} = \sqrt{\sum_{k=1}^{5} \left(G_k^{(i)} - G_k^{(q)}\right)^2 / \sigma_{G_k}^2}, \tag{6}$$

where each component is normalized by its standard deviation σ_{G_k}. Then the spatial reconstruction of the magnetic field for the event of interest is made using only a small $k_{NN} \ll k_{SS}$ part of the state-space with $k_{SS} \sim 4 \cdot 10^6$ points. Since the number of state-space points, k_{SS}, is quite large, the number of our instance-based subset k_{NN} can also be made sufficiently large to use for the magnetic field reconstruction a sufficiently flexible model with many degrees of freedom, which is described in the next section. The specific value of $k_{NN} = 32,000$ used in this study was found before (Stephens et al., 2019; Sitnov et al., 2019) to provide good validation results and resolve the spatial structure of the magnetic field and its evolution during substorms without overfitting.

Fitting the magnetic field data from the kNN subset is made by minimizing the distance in another, magnetic field vector space:

$$M_{err}^{(NN)} = \sqrt{\sum_{j \in S_{NN}} \sum_{i=x,y,z} w_j w_{(0)}(r) \left[B_i^{(mod)}(\mathbf{r}^{(j)}) - B_i^{j,obs}\right]^2}, \tag{7}$$

where $B_i^{j,obs}$ is the magnetic field record from the kNN subset S_{NN} (note that the number of observations in that subset is in general different from the number k_{NN}, because its depends on the number of probes available at any moment in time averaged over the subset;

the data structure of the database by mission is described in Table S1) and $B_i^{(mod)}(\mathbf{r}^{(j)})$ is the value of the jth magnetic field component of the model in the point of observation $\mathbf{r}^{(j)}$.

Note that the data points in the objective function eq. (7) are additionally weighted by the factor $w_{(0)}$ to mitigate the inhomogeneity of magnetometer records in the real space, which is seen from Fig. S1. In this weighting procedure, which is described in more detail in (N. A. Tsyganenko & Sitnov, 2007), the data is binned into $0.5R_E$ intervals of the geocentric distance r. Then the weight $w_{(0)}(r)$ is calculated as $\langle \Delta N \rangle / \max\{0.2\langle \Delta N \rangle, \Delta N_i\}$, where ΔN_i is the number of data points in the ith bin and $\langle \Delta N \rangle$ is the average number per bin over the entire set.

Another weighting w_j has been applied to mitigate the inhomogeneity of data in the state-space eqs. (1)–(5), with stronger data density for weaker solar wind/IMF input, storm and substorm activity (Stephens et al., 2020):

$$w_j = \exp\left[-\left(R_q^{(j)}/\sigma R_{NN}\right)^2/2\right], \tag{8}$$

where R_{NN} is the radius of the NN sphere. The specific value of the weighting parameter $\sigma = 0.3$ used in this study was found in earlier studies to improve the spatial reconstruction and avoid overfitting for the chosen value of k_{NN} (Stephens et al., 2020).

Model Magnetic Field Architecture and Fitting Features

The analytical description of the magnetospheric magnetic field used in this study is nearly identical to that of earlier empirical reconstructions of substorms and is described in more detail in (Stephens et al., 2019). The total magnetospheric magnetic

field, $\mathbf{B}_{tot}$ can be described as a summation of fields owing to individual current systems: $\mathbf{B}_{tot} = \mathbf{B}_{int} + \mathbf{B}_{FAC} + \mathbf{B}_{eq} + \mathbf{B}_{MP}$. The internal field, $\mathbf{B}_{int}$, is fundamentally different than the external fields as it is generated by currents deep in the Earth's interior, possesses a relatively slow rate of change (on the order of years), and is readily measured by ground based magnetometers. For these reasons, $\mathbf{B}_{int}$ is not considered within the scope of magnetospheric research and is represented by the IGRF model (Alken et al., 2021). Of interest are the magnetic fields generated by currents flowing within geospace, termed the external field, $\mathbf{B}_{ext}$. Specifically here, assuming the magnetopause as a perfectly conducting layer, the set of current systems is limited to those flowing within the magnetopause, the field-aligned currents $\mathbf{B}_{FAC}$ and equatorial currents $\mathbf{B}_{eq}$, and on the magnetopause $\mathbf{B}_{MP}$.

The building block for the equatorial current systems is the general solution of an infinitely thin arbitrarily distributed current sheet as detailed by (N. A. Tsyganenko & Sitnov, 2007). Solved in cylindrical coordinates (ρ,ϕ,z), the solution is composed of a Fourier series in ϕ and a Fourier-Bessel series in ρ, and the resulting magnetic field, $\mathbf{B}_{sheet}$, is given by a basis function expansion having the form:

$$\mathbf{B}_{sheet}(\rho, \phi, z) = \sum_{n=1}^{N} a_{0n}^{(s)} \mathbf{B}_{0n}^{(s)} + \sum_{m=1}^{M} \sum_{n=1}^{N} (a_{mn}^{(o)} \mathbf{B}_{mn}^{(o)} + a_{mn}^{(e)} \mathbf{B}_{mn}^{(e)}). \tag{9}$$

where $\mathbf{B}_{0n}$, $\mathbf{B}_{mn}^{(o)}$, and $\mathbf{B}_{mn}^{(e)}$ are basis functions with axially symmetry, odd (sine), and even (cosine) symmetry respectively; while a_{mn} are the amplitude coefficients.

Note, although this yields an arbitrary description in ρ and ϕ, its structure in z is rigidly defined to be an infinitely thin current sheet at $z = 0$. However, the Dirac delta profile of

the current density in z can be broadened into a realistic finite distribution by performing the variable substitution $\zeta = \sqrt{z^2 + D^2}$, introducing the parameter D as the current sheet half-thickness. The thickness parameter D need not be a constant but can take the form of any differentiable function $D = D(\rho, \phi)$.

A distinctive feature of the tail is the formation of multiscale current sheets in the substorm growth phase with an ion-scale thin current sheet (TCS) embedded into a much thicker current sheet (Sergeev et al., 2011). In order to capture this feature, (Stephens et al., 2019) used two such expansions to describe the equatorial field:

$$\mathbf{B}^{(eq)}(\rho, \phi, z) = \mathbf{B}^{(eq)}(\rho, \phi, z; D) + \mathbf{B}^{(eq)}(\rho, \phi, z; D_{TCS}), \tag{10}$$

where D_{TCS} is constrained to be $D_{TCS} < D$. Further studies (Stephens et al., 2019; Sitnov et al., 2019) confirmed the buildup of TCS in the growth phase of substorms and their decay during the expansion and recovery phases.

Earlier studies assumed a spatially constant TCS thickness, $D_{TCS} = const$, although it was allowed to vary in time (Stephens et al., 2019). Here, the embedded TCS structure has been further generalized to verify the possible physical mechanisms of the TCS formation. It can be explained, e.g., (Sitnov et al., 2006), by figure-eight like (Speiser) proton orbits (Speiser, 1965). If this is the case, the parameter D_{TCS} of the magnetic field model should depend on the distance ρ from the Earth because the Speiser orbit size, ρ_{Si}, is inversely proportional to the magnetic field outside the sheet, B_L, which itself depends on ρ (Wang et al., 2004). To take this effect into account, the magnetic field architecture was further

generalized using the approximation eq. (11) with free parameters α, β and D_0 and x_0 to be inferred from data.

$$D_{TCS}(x,y) = \left(\alpha e^{-\beta\rho'} + D_0^{-1}\right)^{-1}, \rho' = \sqrt{(x-x_0)^2 + y^2}. \quad (11)$$

The results of the fitting the TCS thickness model eq. (11) with data within the framework of the DM-based global magnetic field reconstruction using a generalization of the basis-function expansion eq. (9) for variable TCS thickness (eqs.(15)-(17) in (N. A. Tsyganenko & Sitnov, 2007)) are presented in Fig. S2 for the main group of IDR events, G, M, W, and Y. Similar profiles of the lobe field B_L and the inverse TCS thickness D_{TCS} seen in this figure suggest that the TCS thickness scales as the thermal ion gyroradius in the field B_L and hence its is likely formed by quasi-adiabatic (Speiser) ions (Speiser, 1965; Sitnov et al., 2006). The value of D_{TCS} asymptotically approaches D_0 at increasing distance, with the constraint $D_0 \leq D$, so that D_{TCS} cannot exceeds the thickness of the thick sheet.

A further complication is that the equatorial current system rarely lies in a plane centered about $z = 0$. The Earth's dipole axis is not generally orthogonal to the direction of the solar wind flow. The angle that the dipole axis makes with the Z axis of the Geocentric Solar Magnetic (GSM) coordinate system is the "dipole tilt angle". Its finite value may cause bending and warping of the tail current sheet while changes in the IMF clock angle (the angle between geomagnetic north and the projection of the IMF vector onto the GSM Y-Z plane) may twist the current sheet (N. A. Tsyganenko & Fairfield, 2004). These effects can be accounted for by application of the general deformation tech-

nique (N. A. Tsyganenko, 1998). Specifically, here the "bowl-shaped" deformation from (N. A. Tsyganenko, 2014) is used, introducing three additional free parameters which define the center of the current sheet; the hinging distance R_H, the warping parameter G, and the twisting parameter TW.

The values of M and N determine the number of azimuthal and radial expansions in equation (9) and thus the resolution of the equatorial currents in ϕ and ρ respectively. Here, as with previous substorm investigations (Stephens et al., 2019), $(M, N) = (6, 8)$ as this was determined a sufficient resolution to resolve current structure throughout the near and mid-tail without overfitting to data (Stephens & Sitnov, 2021). Further, as with the prior investigations, in order to account for potential dynamical pressure effects on the structure of equatorial currents, each of the amplitude coefficient terms in eq. (9) are made explicit functions of P_{dyn}: $a^{(\gamma)}_{\alpha\beta} \rightarrow a^{(\gamma)}_{0,\alpha\beta} + a^{(\gamma)}_{1,\alpha\beta}\sqrt{P_{dyn}}$, doubling their number. The end result is a total of 416 amplitude coefficients which determine the spatial structure of the equatorial current sheet.

The FAC magnetic field, $\mathbf{B}_{FAC}$, module used in this study is identical to that of (Stephens et al., 2019). The foundation of their analytical description are the radially flowing conical current systems developed in (N. Tsyganenko, 1991), which are then bent to follow approximately dipolar field lines using the general deformation technique which also accounts for the day-night asymmetry (N. A. Tsyganenko, 2002a). The azimuthal dependence of the conical currents utilizes a Fourier series, giving them flexibility to reconstruct the magnetic local time variations of the FACs but at the expense of having a very rigid latitudinal structure. In order to mimic expansion like flexibility in latitude, four

such conical current systems are placed at overlapping latitudes. The first four Fourier terms are used for each of the four latitudinal varying conical currents resulting in a total of 16 linear amplitude coefficients that determine the FACs spatial structure. Global rescaling parameters were introduced to allow the FACs to shrink and grow in response to storm and substorm phases. Instead of allowing each of the four current systems to rescale independently, the two higher latitude systems were tied to one parameter κ_{R1} and the two lower to another κ_{R2}. The values of κ_{R1} and κ_{R2} were constrained so that they approximated the region-1 and region-2 current systems respectively. This formulation was shown to successfully reproduce the more complex spiral like FAC pattern observed in the AMPERE data (Sitnov et al., 2017).

Unlike the other external fields, in which the magnetic field sought is consistent with some conceptualization of a current system, the magnetopause magnetic field, $\mathbf{B}_{MP}$, does not attempt to represent a current. Instead, the domain of validity of the model is restricted to just inside the magnetopause current layer, where $\mathbf{j}_{MP} = 0$. Thus, $\mathbf{B}_{MP}$ is irrotational and can be represented by a magnetic scalar potential, $\mathbf{B}_{MP} = -\nabla U$ and its formulation is simply the solution to Laplace's equation: $\nabla^2 U = 0$ (N. A. Tsyganenko, 2014). In this context, $\mathbf{B}_{MP}$ is termed a shielding field in that it ensures the magnetosphere is closed, that is, that field lines do not cross the magnetopause. A closed magnetosphere is represented by the condition $\mathbf{B}_{tot} \cdot \mathbf{n}|_S = 0$, where S is the modeled magnetopause boundary and $\mathbf{n}$ is the normal to that surface. Here, as with previous studies, S is defined as the Shue magnetopause (Shue et al., 1998). In practice it is more tractable to represent $\mathbf{B}_{MP}$ as a combination of shielding fields: $\mathbf{B}_{MP} = \mathbf{B}_{int}^{(sh)} + \mathbf{B}_{FAC}^{(sh)} + \mathbf{B}_{eq}^{(sh)}$; that

way, each shielding field can be formulated independently using a coordinate system and geometry that makes sense for that particular system. For example, owing to the cylindrical geometry of $\mathbf{B_{eq}}$, U_{eq} is represented by an expansion of Fourier-Bessel harmonics, eq. 20 of (N. A. Tsyganenko & Sitnov, 2007), while U_{int} and U_{FAC} utilize an expansion of "Box" harmonics, appendix of (N. A. Tsyganenko, 1998) and eq. 34 of (N. A. Tsyganenko, 1995) respectively. S is then sampled to a distance of $r \sim 50R_E$ and the shielding field expansion (e.g., $\mathbf{B}_{eq}^{(sh)} = -\nabla U_{eq}$) and the shielded field (e.g., $\mathbf{B_{eq}}$) are evaluated at the location of each sample. This allows the coefficients of the shielding field expansion (e.g. U_{eq}) to be found by minimizing the normal component of the combined field at the magnetopause boundary, e.g., $\min\left[(\mathbf{B}_{eq,j} + \mathbf{B}_{eq,j}^{(sh)}) \cdot \mathbf{n}_j\right]$. For a more thorough discussion on this topic see (N. A. Tsyganenko, 2014).

One more consideration built into the structure of the model is the magnetosphere's expansion and contraction in response to changes in the solar wind dynamical pressure, P_{dyn}. It is well established from observations of magnetopause crossings that the magnetopause responds to decreases/increases in the solar wind dynamical pressure, P_{dyn}, by expanding/contracting in a self-similar way, that is, its size changes but not its shape, e.g., (Sibeck et al., 1991; Shue et al., 1998). This self-similarity is easily represented by rescaling the position vector as a function of P_{dyn}. Using simple pressure balance considerations the functional form of this rescaling is $\mathbf{r}' = {P_{dyn}}^{-\kappa}$, where $\kappa = 1/6$ for a perfect dipole (Mead & Beard, 1964). Here, as with many previous empirical studies, all current systems are assumed to possess the same self-similarity rescaling, that is they all take the same functional form and same value of κ (N. A. Tsyganenko, 2014). This assumption

simplifies the shielding of these fields as both the shielded and the shielding fields rescale together. κ could be treated as a free parameter when the model is fit to data, however, previous studies have shown κ to be relatively stable (N. A. Tsyganenko, 2002b), so here a constant value of $\kappa = 0.155$ from (N. A. Tsyganenko & Sitnov, 2007) was used.

The final magnetic field model configuration includes 432 linear amplitude coefficients and 10 free non-linear parameters D,α,β,D_0,x_0,R_H,G,TW,κ_{R1},κ_{R2} which are determined by fitting them to the identified subset of magnetometer data. The linear coefficients are determined by applying the singular value decomposition pseudo-inversion method to the overdetermined linear least squares problem (Jackson, 1972; Press et al., 1992). The non-linear parameters are found by embedding the linear solver within the Nelder-Mead downhill simplex algorithm (Nelder & Mead, 1965).

Ion Diffusion Region Alphabet

The whole set of 26 IDR events detected by MMS in 2017–2020 (A. J. Rogers et al., 2019; A. Rogers et al., 2021) (labeled in our study by letters A-Z) are listed in Table S2. The second column in the table lists the starting date and time of each IDR interval suggested by MMS (A. J. Rogers et al., 2019; A. Rogers et al., 2021), while the third column indicates the corresponding model time resulting from the adopted 5-min cadence. The forth and fifth columns show the distances between the MMS tetrahedron and reconstructed contours $B_z = 0$ nT and $B_z = 2$ nT. The distance is found as the minimum radius of the 3D sphere, which crosses the corresponding $B_z = const$ contour.

Based on this, we can categorize our 16 "Hits" as $D_{0nT} < 2.0R_E$, which includes 11 X-lines (A, C, D, E, G, Q, S, V, W, X, Y) and 5 O-lines (H, L, M, O, R). "Near hits"

would then be events that miss the 0 nT contour, but instead hit the 2 nT, $D_{2nT} < 2.2R_E$ ($<$ 2 nT for all events except N). This would give us 8 more "Near hits" (I, J, K, N, P, T, U, Z). Our 2 "Misses" (B, F) are then events where both $D_{0nT} \geq 2.0R_E$ and $D_{2nT} \geq 2.2R_E$. These quantitative estimates support the qualitative characterization of the DM fidelity in the $B_z = 0$ contour reconstruction provided in the main text of the paper. The sixth column indicates the figures where the corresponding IDRs are plotted against the corresponding equatorial B_z and meridional current distributions.

Additional IDR Hits

Figs. S3–S8 and S9–S14 show the results of the comparison of the equatorial and meridional magnetic field distributions with the locations of MMS IDRs (A. J. Rogers et al., 2019; A. Rogers et al., 2021) in the formats similar to Figs. 2 and 3 for the rest of the IDR alphabet.

Special considerations were taken in regards to events R and T. In the first case, the initial reconstruction placed the location of the central plasma sheet $\sim 3R_E$ below the MMS spacecraft during the IDR observation. Upon further inspection, the event was found to have an anomalously large value of B_y^{IMF} over the preceding 30-min, with a value of $8nT$. Large magnitudes of y component of the IMF are known to significantly impact the shape of the magnetotail specifically through the twisting of the plasma sheet (N. A. Tsyganenko & Fairfield, 2004). Although this feature is included in the structure of the model through the warping and twisting deformation equations, specifically via the parameter TW in (N. A. Tsyganenko, 1998), its impact is presumably not captured in the storm/substorm state-space represented by eqs. (1)–(5). Indeed, computing TW using

the empirical relationship from (N. A. Tsyganenko & Fairfield, 2004) (see their eq. 1 and eq. 5), results in $TW = 1.11 \times 10^{-2}$, the largest magnitude across all 26 events and being a factor of two larger than the next highest and a factor of five higher than the average event. Thus, event R was reconstructed using this empirical value and not the value obtained during the fit ($TW = 2.64 \times 10^{-3}$). As earlier studies using the SST19 model were primarily concerned with the inner magnetosphere and/or the near-tail region, they probably neglected to observe this inconsistency. In future studies, particularly of the mid-tail, this issue should be remedied. One potential solution is to explicitly add a dimension to the state-space that correlates to the twisting effect, for instance the value of B_y^{IMF} itself or the IMF clock angle. However, owing to the "curse of dimensionality" (Verleysen & François, 2005), expanding the state-space may dilute its sensitivity to the storm and substorm features sought. Another solution that is potentially more robust is to exclude TW from the set of free parameters that is determined when fitting to data and instead replace it with an ad-hoc functional form such as the empirical relationship from (N. A. Tsyganenko & Fairfield, 2004).

In event T, the original reconstruction with $\sigma = 0.3$ underresolved the X-line, apparently because of the unusual IMF structure ($|B_z| \sim |B_x| \sim |B_y| \sim 6$ nT). To mitigate this issue, we slightly reduced the weighting parameter to $\sigma = 0.25$.

References

Alken, P., Thébault, E., Beggan, C. D., Amit, H., Aubert, J., Baerenzung, J., ... Zhou, B. (2021, December). International geomagnetic reference field: the thirteenth generation. *Earth, Planets and Space*, *73*(1), 49. doi: 10.1186/s40623-020-01288-x

Burton, R. K., McPherron, R. L., & Russell, C. T. (1975). An empirical relationship between interplanetary conditions and dst. *Journal of Geophysical Research (1896-1977)*, *80*(31), 4204-4214. doi: https://doi.org/10.1029/JA080i031p04204

Gjerloev, J. W. (2012). The supermag data processing technique. *Journal of Geophysical Research: Space Physics*, *117*(A9), https://doi.org/10.1029/2012JA017683. doi: https://doi.org/10.1029/2012JA017683

Gonzalez, W. D., Joselyn, J. A., Kamide, Y., Kroehl, H. W., Rostoker, G., Tsurutani, B. T., & Vasyliunas, V. M. (1994). What is a geomagnetic storm? *Journal of Geophysical Research: Space Physics*, *99*(A4), 5771-5792. Retrieved from `https://agupubs.onlinelibrary.wiley.com/doi/abs/10.1029/93JA02867` doi: https://doi.org/10.1029/93JA02867

Jackson, D. D. (1972, 06). Interpretation of Inaccurate, Insufficient and Inconsistent Data. *Geophysical Journal International*, *28*(2), 97-109. Retrieved from `https://doi.org/10.1111/j.1365-246X.1972.tb06115.x` doi: 10.1111/j.1365-246X.1972.tb06115.x

Li, T., Priest, E., & Guo, R. (2021). Three-dimensional magnetic reconnection in astrophysical plasmas. *Proc. Royal Soc. A*, *477*(2249), 10.1098/rspa.2020.0949. doi: 10.1098/rspa.2020.0949

Liemohn, M. W., McCollough, J. P., Jordanova, V. K., Ngwira, C. M., Morley, S. K., Cid, C., ... Vasile, R. (2018). Model evaluation guidelines for geomagnetic index predictions. *Space Weather*, *16*(12), 2079-2102. Retrieved from `https://agupubs.onlinelibrary.wiley.com/doi/abs/10.1029/2018SW002067` doi: https://doi

.org/10.1029/2018SW002067

Mead, G. D., & Beard, D. B. (1964). Shape of the geomagnetic field solar wind boundary. *Journal of Geophysical Research (1896-1977)*, *69*(7), 1169-1179. Retrieved from https://agupubs.onlinelibrary.wiley.com/doi/abs/10.1029/JZ069i007p01169 doi: https://doi.org/10.1029/JZ069i007p01169

Nelder, J. A., & Mead, R. (1965, 01). A Simplex Method for Function Minimization. *The Computer Journal*, *7*(4), 308-313. Retrieved from https://doi.org/10.1093/comjnl/7.4.308 doi: 10.1093/comjnl/7.4.308

Newell, P. T., & Gjerloev, J. W. (2011). Evaluation of supermag auroral electrojet indices as indicators of substorms and auroral power. *Journal of Geophysical Research: Space Physics*, *116*(A12), https://doi.org/10.1029/2011JA016779. Retrieved from https://agupubs.onlinelibrary.wiley.com/doi/abs/10.1029/2011JA016779 doi: https://doi.org/10.1029/2011JA016779

Newell, P. T., & Gjerloev, J. W. (2012). Supermag-based partial ring current indices. *Journal of Geophysical Research: Space Physics*, *117*(A5), https://doi.org/10.1029/2012JA017586. Retrieved from https://agupubs.onlinelibrary.wiley.com/doi/abs/10.1029/2012JA017586 doi: https://doi.org/10.1029/2012JA017586

Partamies, N., Juusola, L., Tanskanen, E., & Kauristie, K. (2013). Statistical properties of substorms during different storm and solar cycle phases. *Annales Geophysicae*, *31*(2), 349–358. Retrieved from https://www.ann-geophys.net/31/349/2013/ doi: 10.5194/angeo-31-349-2013

Press, W. H., Teukolsky, S. A., Flannery, B. P., & Vetterling, W. T. (1992). *Numerical recipes in fortran: The art of scientific computing* (2nd ed.). USA: Cambridge University Press.

Rogers, A., Farrugia, C. J., Torbert, R. B., & Rogers, T. J. (2021). Applying magnetic curvature to to MMS data to identify thin current sheets relative to tail reconnection. *Earth and Space Science Open Archive*, 12. doi: 10.1002/essoar.10509282.1

Rogers, A. J., Farrugia, C. J., & Torbert, R. B. (2019). Numerical algorithm for detecting ion diffusion regions in the geomagnetic tail with applications to mms tail season 1 may to 30 september 2017. *Journal of Geophysical Research: Space Physics*, *124*(8), 6487-6503. Retrieved from `https://agupubs.onlinelibrary.wiley.com/doi/abs/10.1029/2018JA026429` doi: https://doi.org/10.1029/2018JA026429

Sergeev, V., Angelopoulos, V., Kubyshkina, M., Donovan, E., Zhou, X.-Z., Runov, A., ... Nakamura, R. (2011). Substorm growth and expansion onset as observed with ideal ground-spacecraft themis coverage. *Journal of Geophysical Research: Space Physics*, *116*(A5), https://doi.org/10.1029/2010JA015689. doi: https://doi.org/10.1029/2010JA015689

Shue, J.-H., Song, P., Russell, C. T., Steinberg, J. T., Chao, J. K., Zastenker, G., ... Kawano, H. (1998). Magnetopause location under extreme solar wind conditions. *Journal of Geophysical Research: Space Physics*, *103*(A8), 17691-17700. doi: https://doi.org/10.1029/98JA01103

Sibeck, D. G., Lopez, R. E., & Roelof, E. C. (1991). Solar wind control of the magnetopause shape, location, and motion. *Journal of Geophysical Re-*

search: Space Physics, *96*(A4), 5489-5495. Retrieved from https://agupubs.onlinelibrary.wiley.com/doi/abs/10.1029/90JA02464 doi: https://doi.org/10.1029/90JA02464

Sitnov, M. I., Sharma, A. S., Papadopoulos, K., & Vassiliadis, D. (2001, Dec). Modeling substorm dynamics of the magnetosphere: From self-organization and self-organized criticality to nonequilibrium phase transitions. *Phys. Rev. E*, *65*, 016116. Retrieved from https://link.aps.org/doi/10.1103/PhysRevE.65.016116 doi: 10.1103/PhysRevE.65.016116

Sitnov, M. I., Stephens, G. K., Tsyganenko, N. A., Miyashita, Y., Merkin, V. G., Motoba, T., ... Genestreti, K. J. (2019). Signatures of nonideal plasma evolution during substorms obtained by mining multimission magnetometer data. *Journal of Geophysical Research: Space Physics*, *124*(11), 8427-8456. doi: 10.1029/2019JA027037

Sitnov, M. I., Stephens, G. K., Tsyganenko, N. A., Ukhorskiy, A. Y., Wing, S., Korth, H., & Anderson, B. J. (2017). Spatial structure and asymmetries of magnetospheric currents inferred from high-resolution empirical geomagnetic field models. In *Dawn-dusk asymmetries in planetary plasma environments* (p. 199-212). American Geophysical Union (AGU). doi: 10.1002/9781119216346.ch15

Sitnov, M. I., Swisdak, M., Guzdar, P. N., & Runov, A. (2006). Structure and dynamics of a new class of thin current sheets. *Journal of Geophysical Research: Space Physics*, *111*(A8), https://doi.org/10.1029/2005JA011517. doi: https://doi.org/10.1029/2005JA011517

Sitnov, M. I., Tsyganenko, N. A., Ukhorskiy, A. Y., & Brandt, P. C. (2008). Dy-

namical data-based modeling of the storm-time geomagnetic field with enhanced spatial resolution. *Journal of Geophysical Research: Space Physics*, *113*(A7), 10.1029/2007JA013003. doi: 10.1029/2007JA013003

Sitnov, M. I., Ukhorskiy, A. Y., & Stephens, G. K. (2012). Forecasting of global data-binning parameters for high-resolution empirical geomagnetic field models. *Space Weather*, *10*(9), 10.1029/2012SW000783. doi: 10.1029/2012SW000783

Speiser, T. W. (1965). Particle trajectories in model current sheets: 1. analytical solutions. *Journal of Geophysical Research (1896-1977)*, *70*(17), 4219-4226. doi: https://doi.org/10.1029/JZ070i017p04219

Stephens, G. K., Bingham, S. T., Sitnov, M. I., Gkioulidou, M., Merkin, V. G., Korth, H., ... Ukhorskiy, A. Y. (2020). Storm time plasma pressure inferred from multimission measurements and its validation using van allen probes particle data. *Space Weather*, *18*(12), e2020SW002583. doi: https://doi.org/10.1029/2020SW002583

Stephens, G. K., & Sitnov, M. I. (2021). Concurrent empirical magnetic reconstruction of storm and substorm spatial scales using data mining and virtual spacecraft. *Frontiers in Physics*, *9*, 210. Retrieved from `https://www.frontiersin.org/article/10.3389/fphy.2021.653111` doi: 10.3389/fphy.2021.653111

Stephens, G. K., Sitnov, M. I., Korth, H., Tsyganenko, N. A., Ohtani, S., Gkioulidou, M., & Ukhorskiy, A. Y. (2019). Global empirical picture of magnetospheric substorms inferred from multimission magnetometer data. *Journal of Geophysical Research: Space Physics*, *124*(2), 1085-1110. Retrieved from `https://agupubs.onlinelibrary.wiley.com/doi/abs/10.1029/2018JA025843` doi: 10.1029/2018JA025843

Tsyganenko, N. (1991). Methods for quantitative modeling of the magnetic field from Birkeland currents. *Planetary and Space Science*, *39*(4), 641 - 654. Retrieved from http://www.sciencedirect.com/science/article/pii/003206339190058I doi: http://dx.doi.org/10.1016/0032-0633(91)90058-I

Tsyganenko, N., Andreeva, V., Kubyshkina, M., Sitnov, M., & Stephens, G. (2021). Data-based modeling of the earth's magnetic field. In *Magnetospheres in the solar system* (p. 617-635). American Geophysical Union (AGU). Retrieved from https://agupubs.onlinelibrary.wiley.com/doi/abs/10.1002/9781119815624.ch39 doi: https://doi.org/10.1002/9781119815624.ch39

Tsyganenko, N. A. (1995). Modeling the earth's magnetospheric magnetic field confined within a realistic magnetopause. *Journal of Geophysical Research: Space Physics*, *100*(A4), 5599-5612. doi: https://doi.org/10.1029/94JA03193

Tsyganenko, N. A. (1998). Modeling of twisted/warped magnetospheric configurations using the general deformation method. *Journal of Geophysical Research: Space Physics*, *103*(A10), 23551-23563. Retrieved from https://agupubs.onlinelibrary.wiley.com/doi/abs/10.1029/98JA02292 doi: https://doi.org/10.1029/98JA02292

Tsyganenko, N. A. (2002a). A model of the near magnetosphere with a dawn-dusk asymmetry 1. Mathematical structure. *Journal of Geophysical Research: Space Physics*, *107*(A8), SMP 12-1-SMP 12-15. doi: 10.1029/2001JA000219

Tsyganenko, N. A. (2002b). A model of the near magnetosphere with a dawn-dusk asymmetry 2. parameterization and fitting to observations. *Jour-*

nal of Geophysical Research: Space Physics, *107*(A8), SMP 10-1-SMP 10-17. Retrieved from https://agupubs.onlinelibrary.wiley.com/doi/abs/10.1029/2001JA000220 doi: https://doi.org/10.1029/2001JA000220

Tsyganenko, N. A. (2014). Data-based modeling of the geomagnetosphere with an imf-dependent magnetopause. *Journal of Geophysical Research: Space Physics*, *119*(1), 335-354. doi: 10.1002/2013JA019346

Tsyganenko, N. A., Andreeva, V. A., Sitnov, M. I., Stephens, G. K., Gjerloev, J. W., Chu, X., & Troshichev, O. A. (2021). Reconstructing substorms via historical data mining: Is it really feasible? *Journal of Geophysical Research: Space Physics*, *126*(10), e2021JA029604. doi: https://doi.org/10.1029/2021JA029604

Tsyganenko, N. A., & Fairfield, D. H. (2004). Global shape of the magnetotail current sheet as derived from geotail and polar data. *Journal of Geophysical Research: Space Physics*, *109*(A3), https://doi.org/10.1029/2003JA010062. doi: https://doi.org/10.1029/2003JA010062

Tsyganenko, N. A., & Sitnov, M. I. (2007). Magnetospheric configurations from a high-resolution data-based magnetic field model. *Journal of Geophysical Research: Space Physics*, *112*(A6), 10.1029/2007JA012260. doi: 10.1029/2007JA012260

Vassiliadis, D. (2006). Systems theory for geospace plasma dynamics. *Reviews of Geophysics*, *44*(2), https://doi.org/10.1029/2004RG000161. doi: https://doi.org/10.1029/2004RG000161

Vassiliadis, D., Klimas, A., & Baker, D. (1999). Models of dst geomagnetic activity and of its coupling to solar wind parameters. *Physics and Chemistry of the Earth, Part C:*

Solar, Terrestrial & Planetary Science, *24*(1), 107-112. Retrieved from https://www.sciencedirect.com/science/article/pii/S1464191798000166 (International Symposium on Solar-Terrestrial Coupling Processes) doi: https://doi.org/10.1016/S1464-1917(98)00016-6

Vassiliadis, D., Klimas, A. J., Baker, D. N., & Roberts, D. A. (1995). A description of the solar wind-magnetosphere coupling based on nonlinear filters. *Journal of Geophysical Research: Space Physics*, *100*(A3), 3495-3512. Retrieved from https://agupubs.onlinelibrary.wiley.com/doi/abs/10.1029/94JA02725 doi: https://doi.org/10.1029/94JA02725

Verleysen, M., & François, D. (2005). The curse of dimensionality in data mining and time series prediction. In J. Cabestany, A. Prieto, & F. Sandoval (Eds.), *Computational intelligence and bioinspired systems* (pp. 758–770). Berlin, Heidelberg: Springer Berlin Heidelberg.

Wang, C.-P., Lyons, L. R., Nagai, T., & Samson, J. C. (2004). Midnight radial profiles of the quiet and growth-phase plasma sheet: The geotail observations. *Journal of Geophysical Research: Space Physics*, *109*(A12), https://doi.org/10.1029/2004JA010590. doi: https://doi.org/10.1029/2004JA010590

Wettschereck, D., Aha, D. W., & Mohri, T. (1997, Feb 01). A review and empirical evaluation of feature weighting methods for a class of lazy learning algorithms. *Artificial Intelligence Review*, *11*(1), 273-314. Retrieved from https://doi.org/10.1023/A:1006593614256 doi: 10.1023/A:1006593614256

Williams, T., Shulman, S., Ottenstein, N., Palmer, E., Riley, C., Letourneau, S., ... Godine, D. (2020). Operational techniques for dealing with long eclipses during the mms extended mission. In *2020 ieee aerospace conference* (p. 1-12). doi: 10.1109/AERO47225.2020.9172276

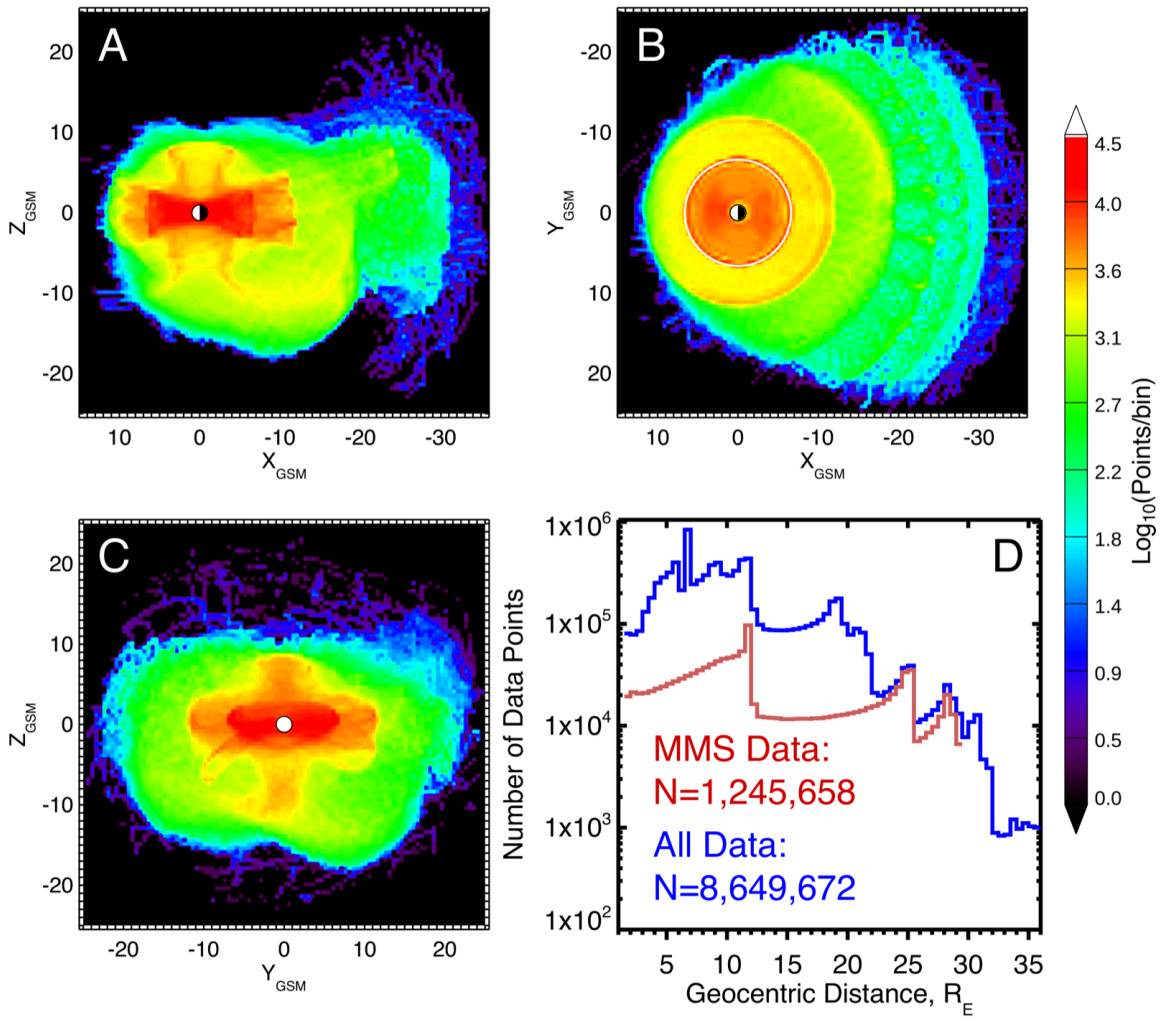

Figure S1. Distribution of data points in the archive of space magnetometer Data. (A, B, and D) A 2D histogram displaying the spatial distribution a data points projected into the meridional (A), equatorial (B), and Y-Z (C) planes in the GSM coordinate system. The color indicates the number of points in each $0.5R_E$ by $0.5R_E$ bin using a logarithmic scale, with red/purple corresponding to regions with a dense/sparse density of data points. Black regions contain zero data points. (D) A 1D histogram showing the number of data points in $0.5R_E$ radial bins (spherical shells) using a logarithmic scale with the total archive in blue and just the MMS dataset in red.

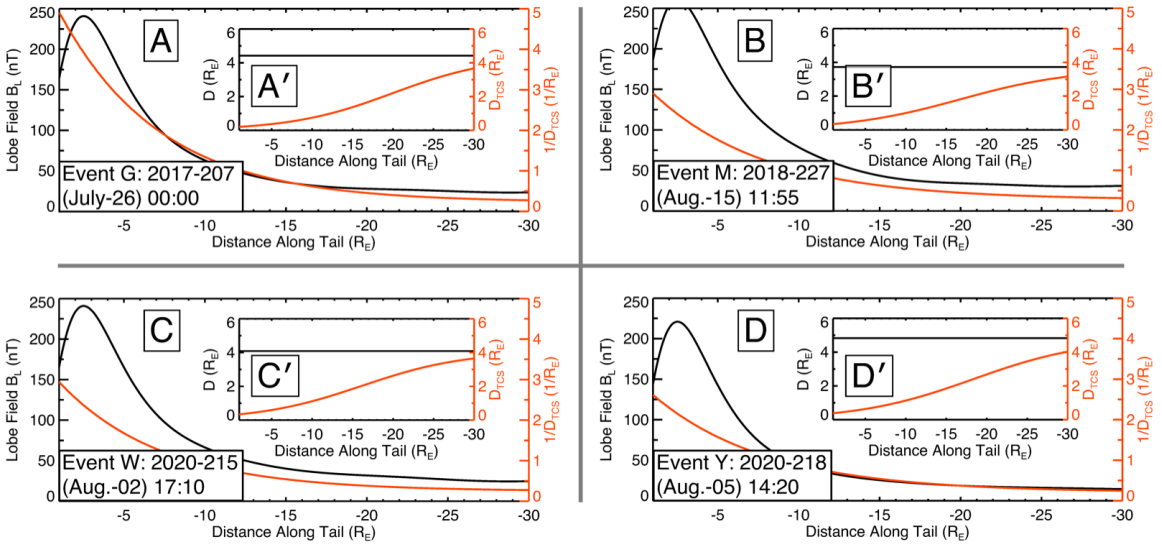

Figure S2. Profiles of the lobe field B_L and current sheet thicknesses along the tail. (A-D) 1D profiles of the for B_L (black line) and the inverse TCS thickness $1/D_{TCS}$ (orange line) sampled at midnight ($y = 0$) along the tail for four IDR events, G, M, W, and Y. B_L is evaluated at a height of $z = 5R_E$ above the center of the current sheet. The inset panels (A'-D') show the value 1D profiles of the current sheet thickness for the thick sheet (black constant line) and D_{TCS} (orange line).

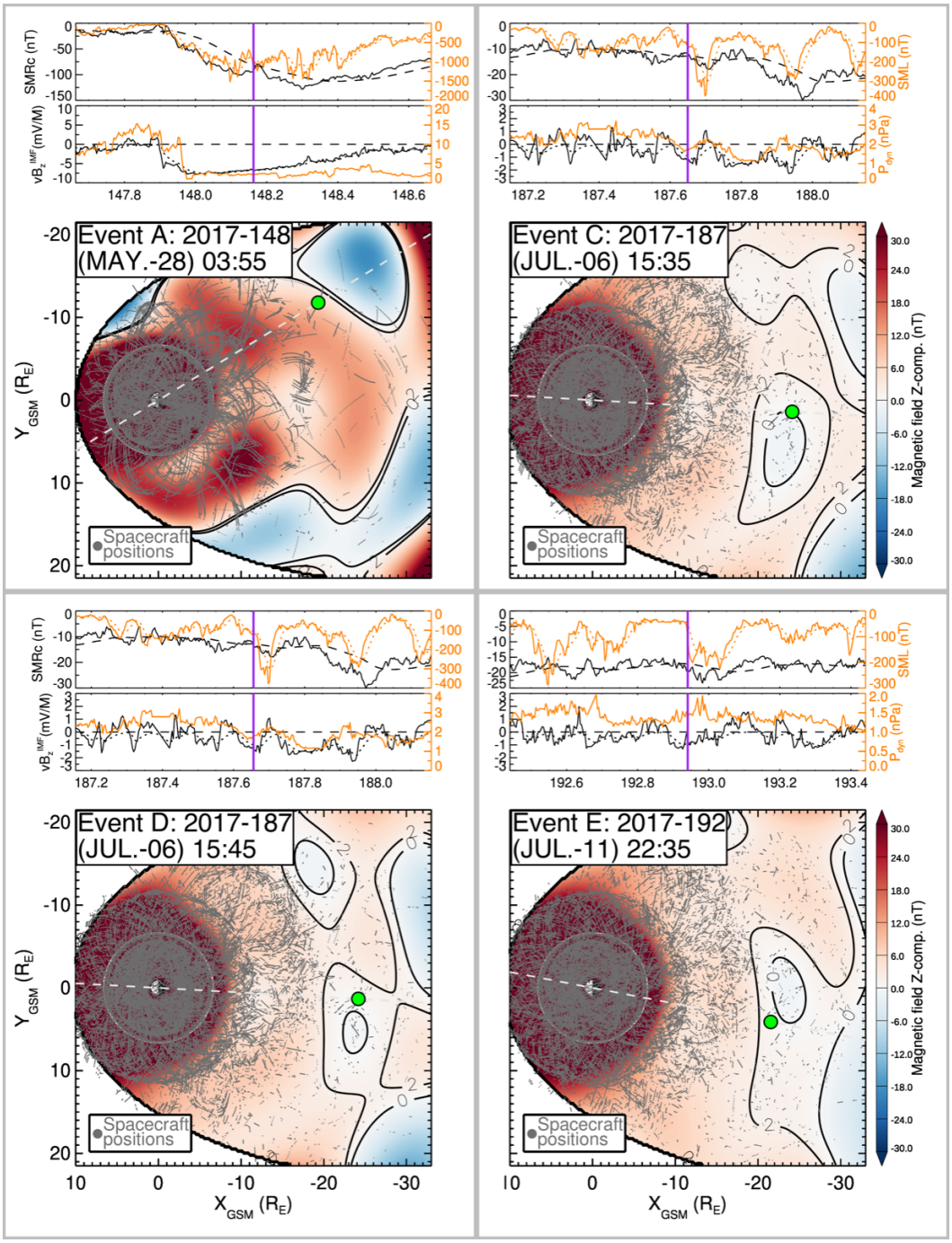

Figure S3. Ion diffusion regions and the equatorial magnetic field landscape. The format is similar to Fig. 2 except for a different group of IDR events: A, C, D, and E, which are marked here by purple dots. These four events are considered "hits" as the $B_z = 0$ contour is within $< 2R_E$ of the observed MMS IDR.

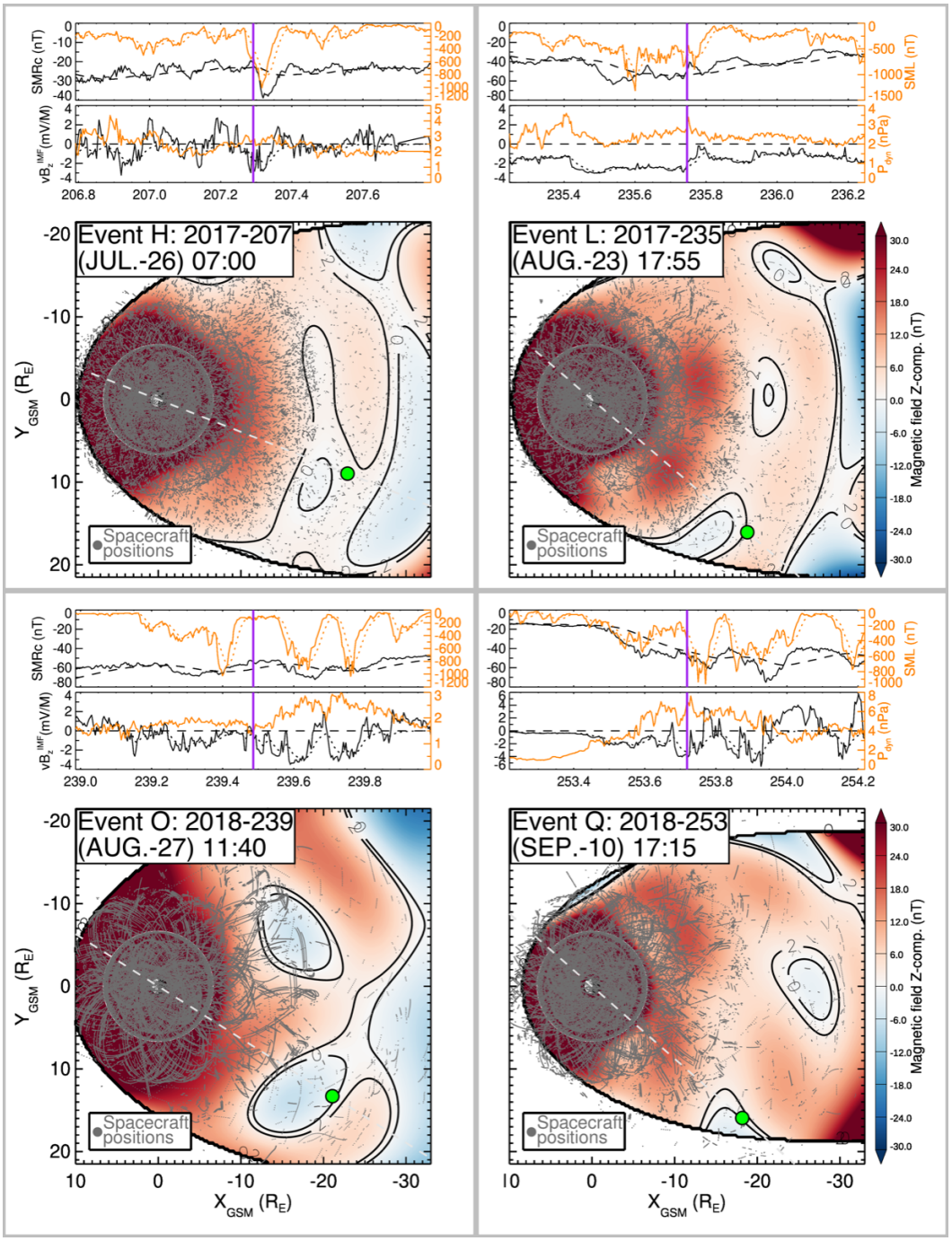

Figure S4. Ion diffusion regions and the equatorial magnetic field landscape. The format is similar to Fig. S3 except for a different group of IDR events: H, L, O, and Q. These four events are considered "hits" as the $B_z = 0$ contour is within $< 2R_E$ of the observed MMS IDR.

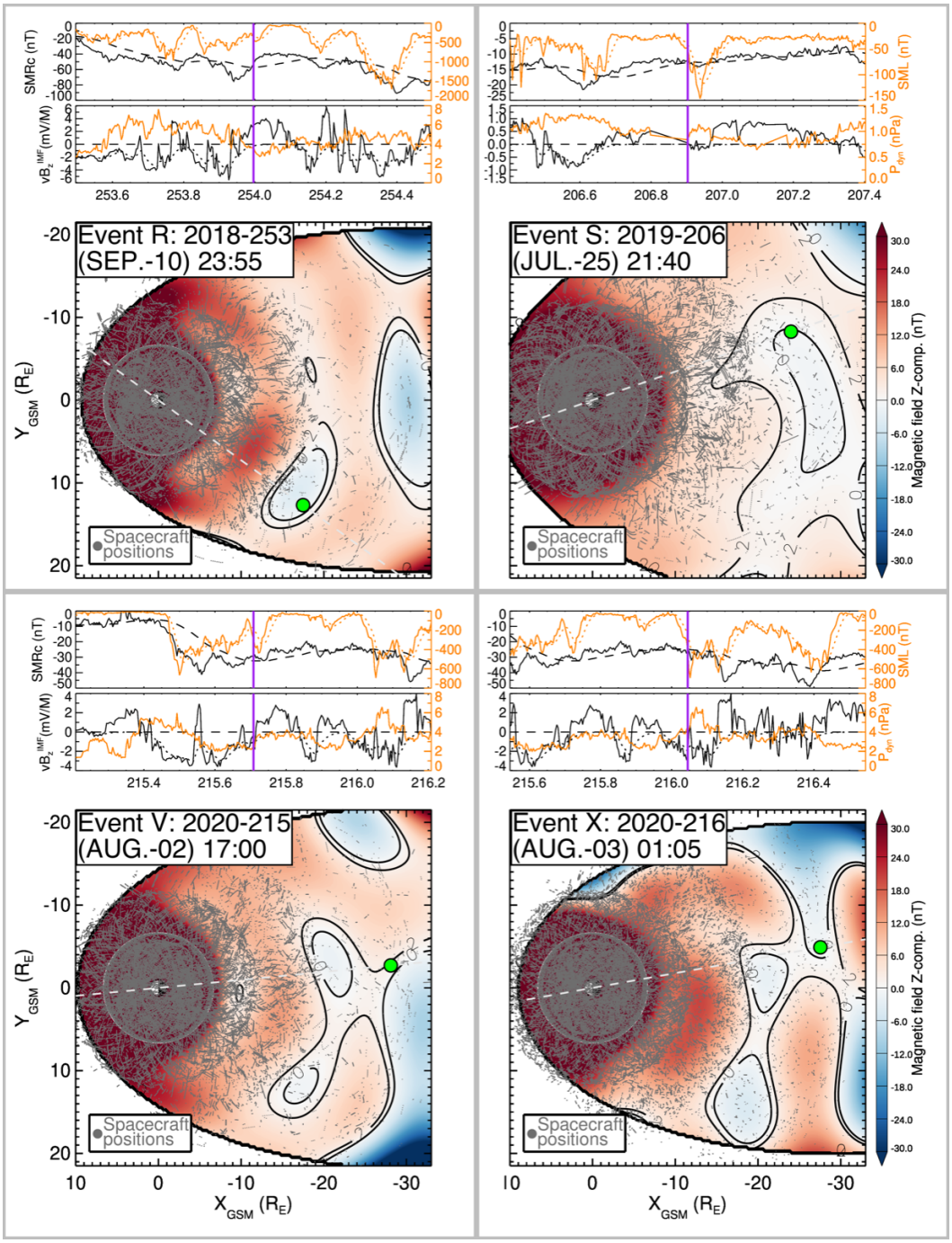

Figure S5. Ion diffusion regions and the equatorial magnetic field landscape. The format is similar to Fig. S3 except for a different group of IDR events: R, S, V, and X. These four events are considered "hits" as the $B_z = 0$ contour is within $< 2R_E$ of the observed MMS IDR.

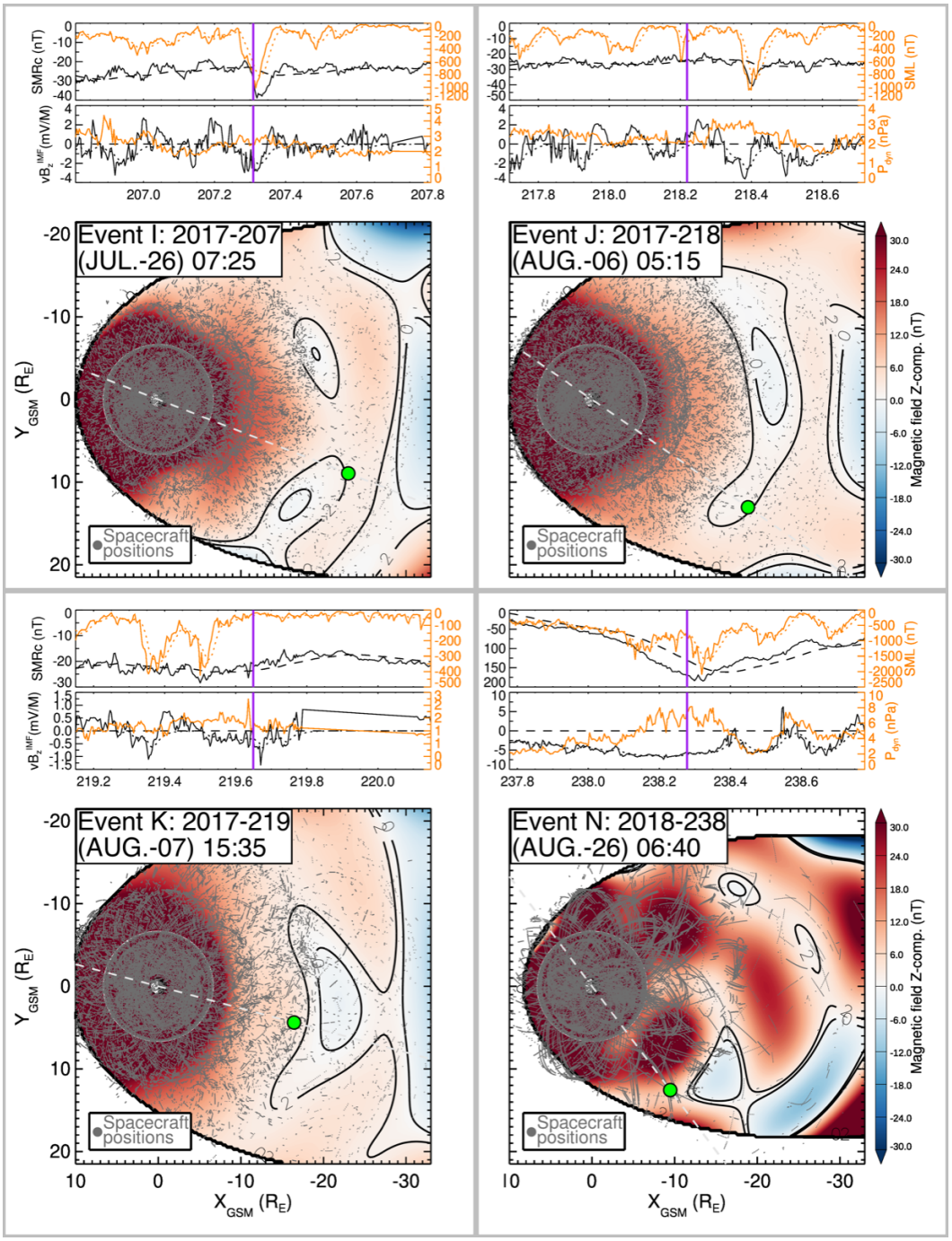

Figure S6. Ion diffusion regions and the equatorial magnetic field landscape. The format is similar to Fig. S3 except for a different group of IDR events: I, J, K, and N. These four events are not as consistent as the 16 "hits", however, the $B_z = 2$ nT is close to the observed MMS IDR for events I, J, and K and is within several R_E for of the $B_z = 0$ contour for events K and N.

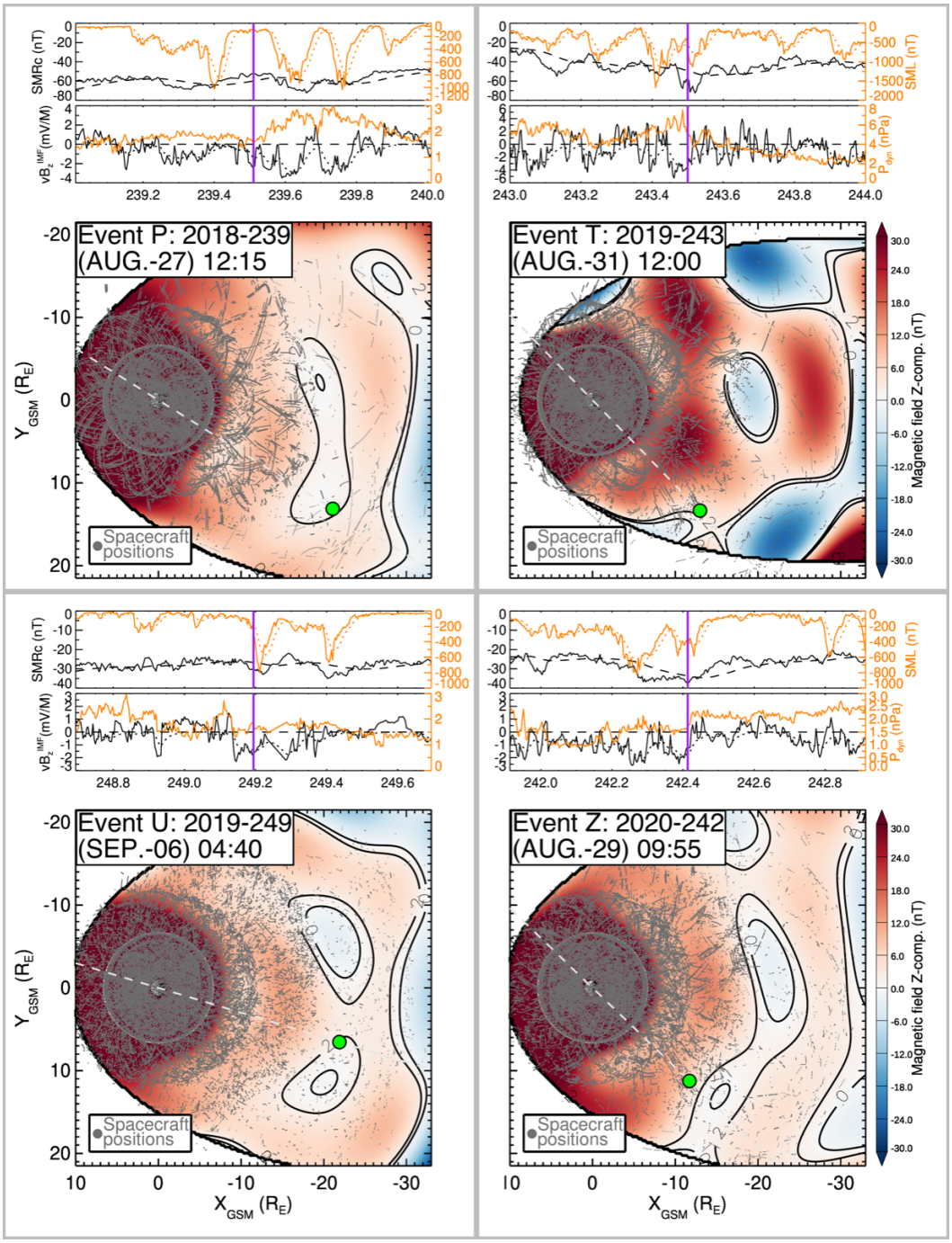

Figure S7. Ion diffusion regions and the equatorial magnetic field landscape. The format is similar to Fig. S3 except for a different group of IDR events, P, T, U, and Z. These four events are considered "near hits" as the $B_z = 2$ nT contour is within $< 2R_E$ of the observed MMS IDR.

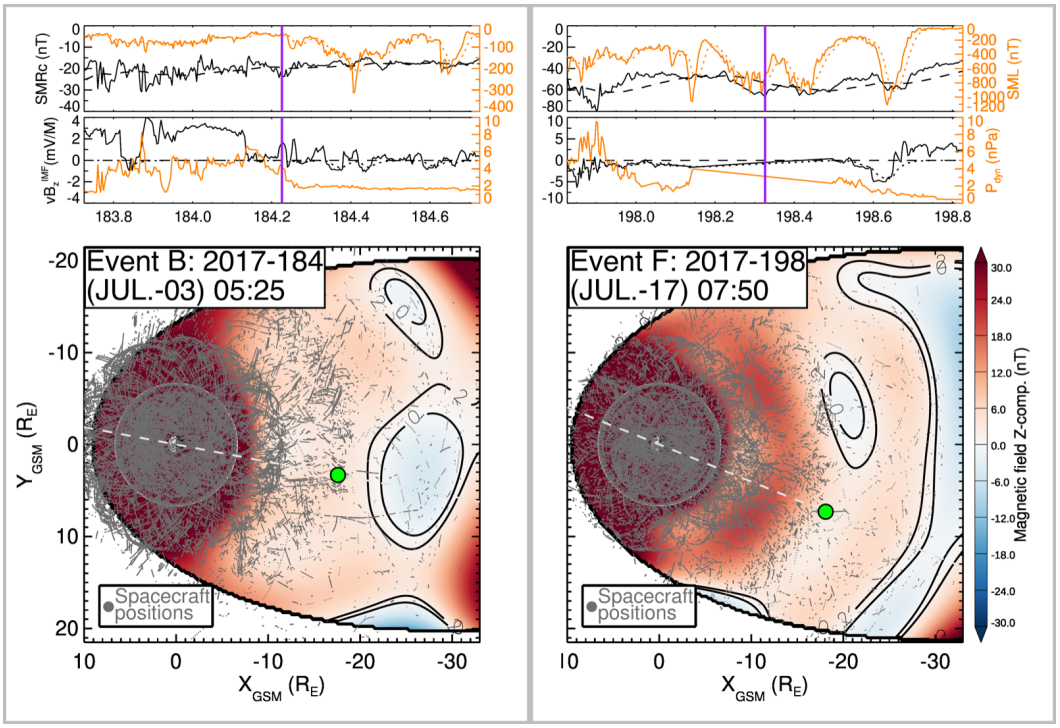

Figure S8. Ion diffusion regions and the equatorial magnetic field landscape. The format is similar to Fig. S3 except for a different group of IDR events B and F when the contours $B_z = 0$ nT and $B_z = 2$ nT are not close to the observed MMS IDR locations.

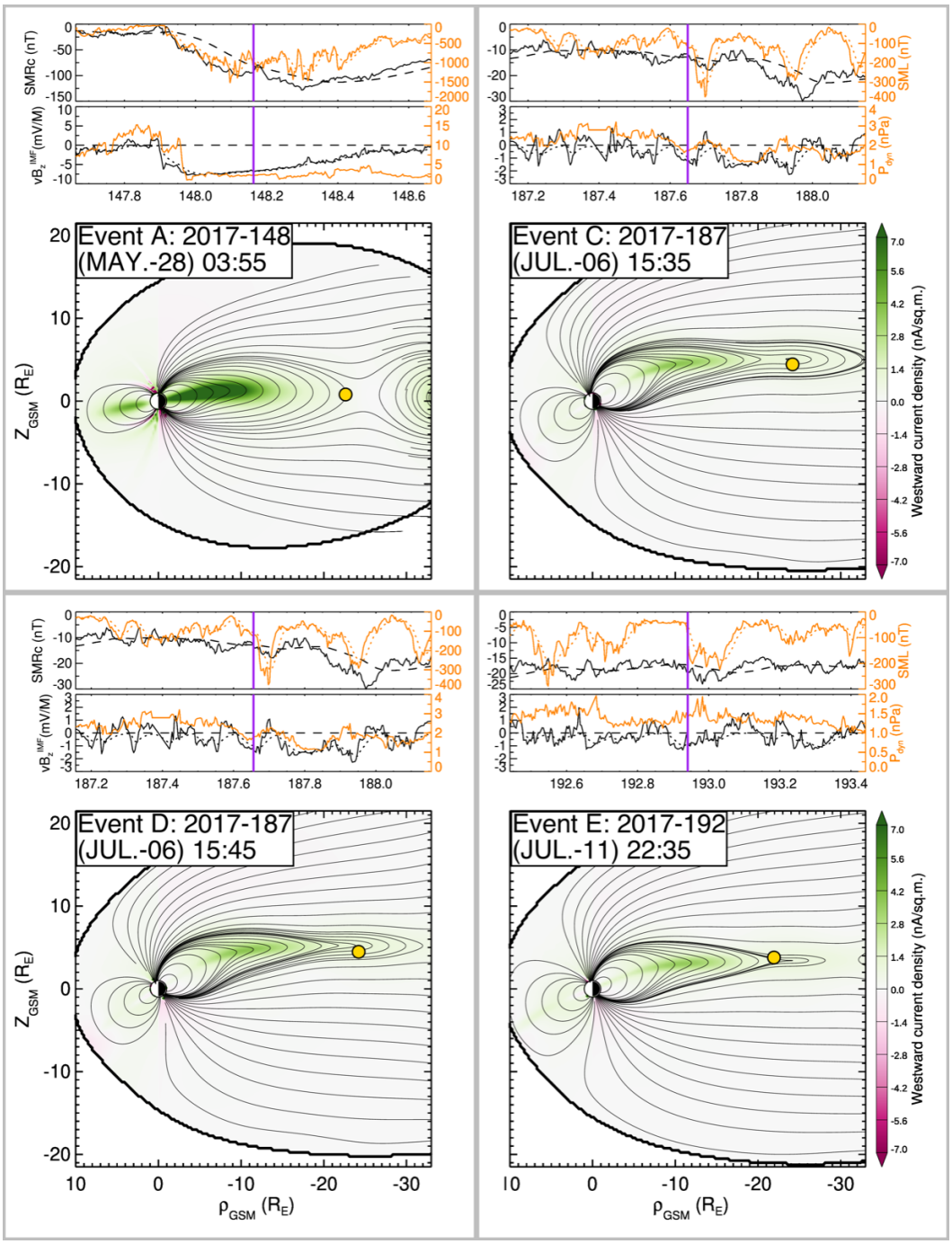

Figure S9. Ion diffusion regions against the meridional current and magnetic field distributions for events A, C, D, and E. The format is similar to Fig. 3, although the MMS IDR locations are marked by the purple dots.

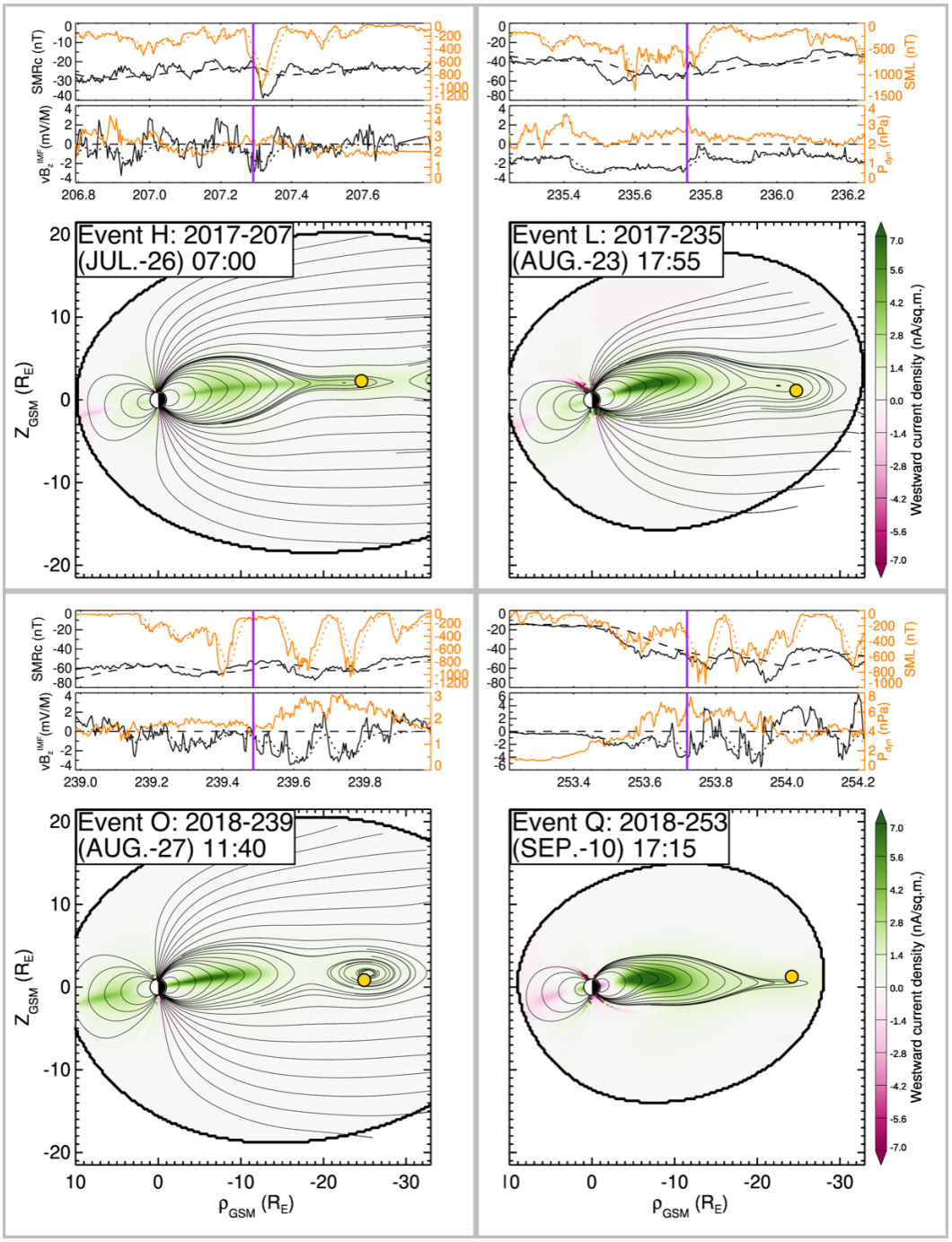

Figure S10. Ion diffusion regions against the meridional current and magnetic field distributions for events H, L, O, and Q. The format is similar to Fig. S9.

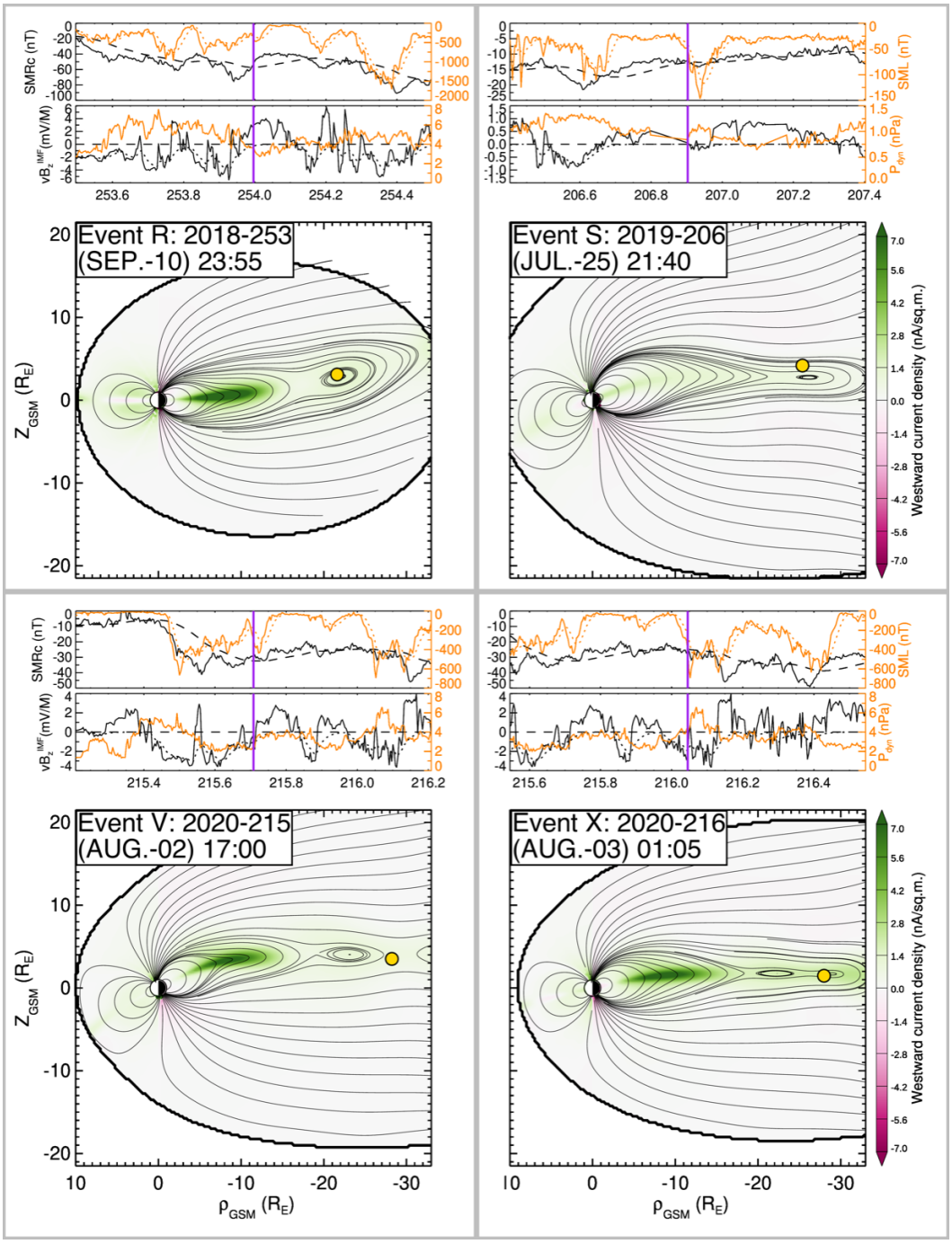

Figure S11. Ion diffusion regions against the meridional current and magnetic field distributions for events R, S, V, and X. The format is similar to Fig. S9.

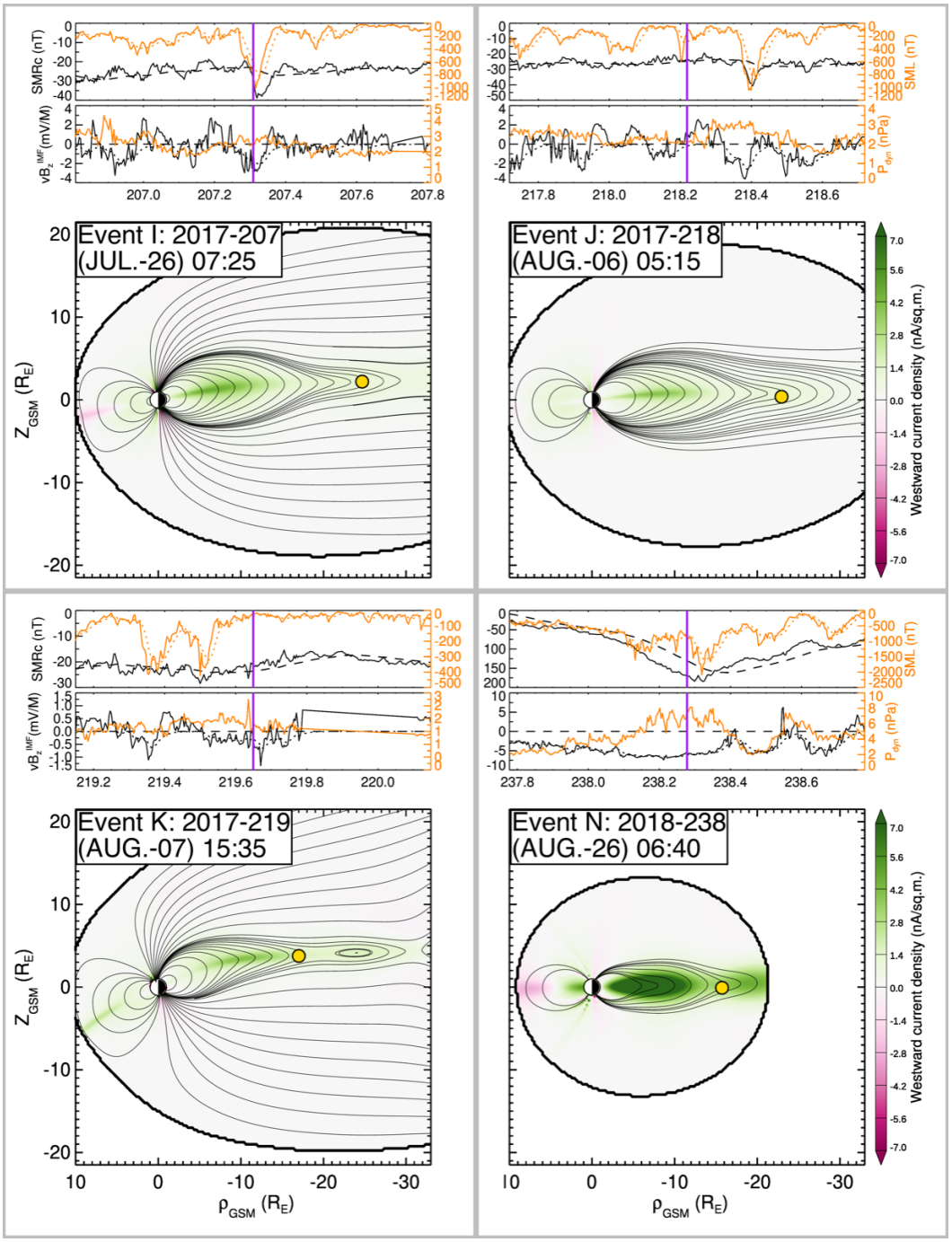

Figure S12. Ion diffusion regions against the meridional current and magnetic field distributions for events I, J, K, and N. The format is similar to Fig. S9.

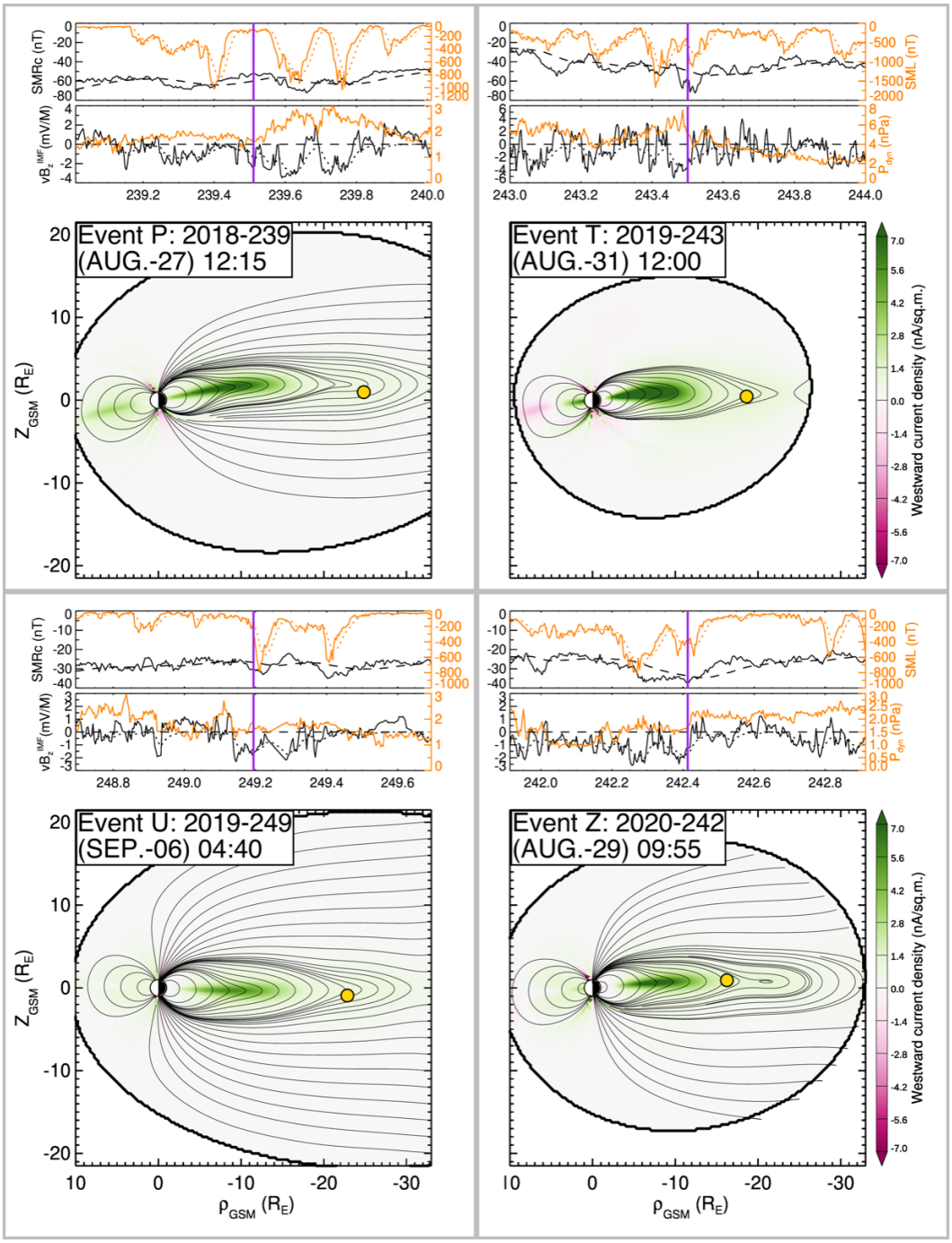

Figure S13. Ion diffusion regions against the meridional current and magnetic field distributions for events P, T, U, and Z. The format is similar to Fig. S9.

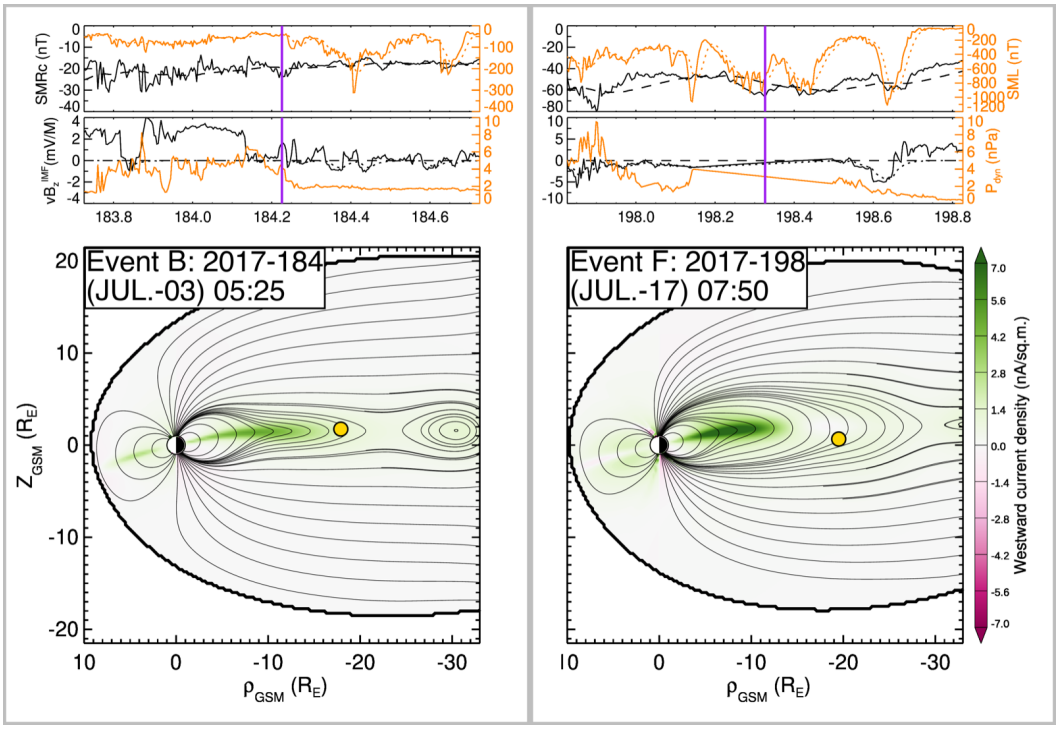

Figure S14. Ion diffusion regions against the meridional current and magnetic field distributions for events B and F. The format is similar to Fig. S9.

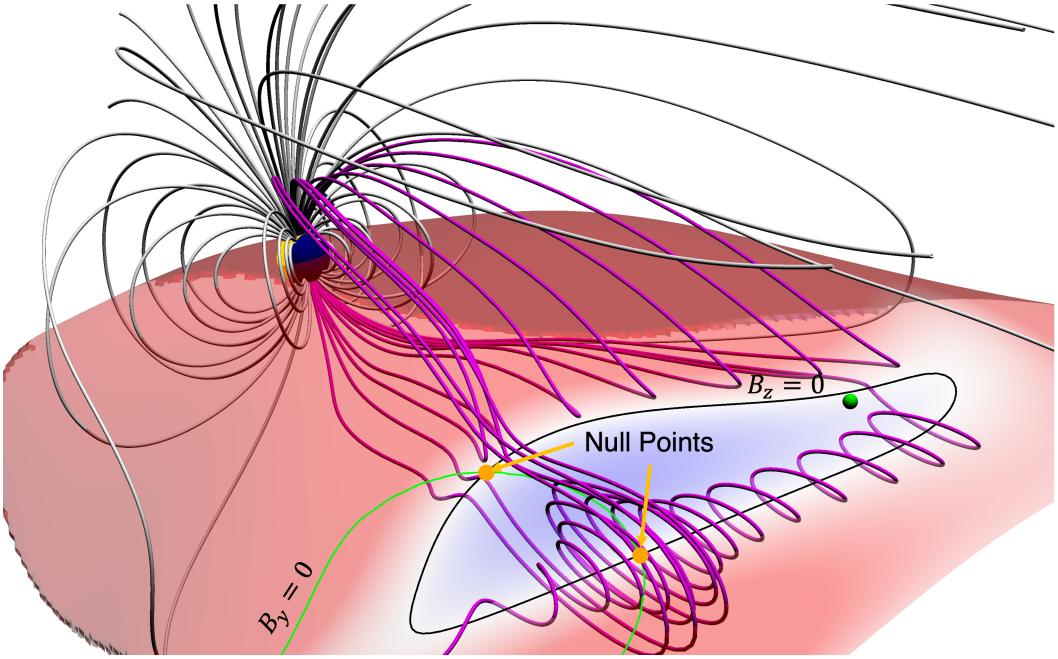

Figure S15. 3D global picture of the magnetosphere with more field lines near the expected magnetic nulls (orange tadpole marks), which are defined as intersections of the surface $B_y = 0$ with the equatorial $B_z = 0$ loop shown in Fig. 1. According to the null nomenclature (Li et al., 2021), the near-Earth and more distant null areas correspond to radial and spiral nulls.

Table S1. The Archive of Space Magnetometer Data.

Spacecraft	Number	Period	Cadence (min)
Cluster 1	756,822	2001–2015	5
Cluster 2	753,580	2001–2015	5
Cluster 3	748,084	2001–2015	5
Cluster 4	561,497	2001–2015	5
Geotail	133,107	1995–2005	15
Polar	844,212	1996–2006	5
IMP-8	10,177	1995–2000	15
GOES-8	233,674	1995–2003	15
GOES-9	84,951	1995–1998	15
GOES-10	213,295	1999–2005	15
GOES-12	79,569	2003–2005	15
THEMIS-A	702,043	2008–2015	5
THEMIS-B	78,523	2008–2011	5
THEMIS-C	115,459	2008–2011	5
THEMIS-D	702,388	2008–2015	5
THEMIS-E	711,441	2008–2015	5
Van Allen A	337,582	2012–2016	5
Van Allen B	337,610	2012–2016	5
MMS 1	312,040	2015–2020	5
MMS 2	312,050	2015–2020	5
MMS 3	311,349	2015–2020	5
MMS 4	310,219	2015–2020	5
Total	8,649,672	1995–2020	5/15

Table S2. The MMS IDR Alphabet.

Event	Start Date/Time	Model Date/Time	$D_{0nT}(R_E)$	$D_{2nT}(R_E)$	Figures
A	2017-05-28T03:57	03:55	1.94	1.40	S3 S9
B	2017-07-03T05:26	05:25	4.72	3.23	S8 S14
C	2017-07-06T15:34	15:35	0.58	3.77	S3 S9
D	2017-07-06T15:45	15:45	1.72	2.54	S3 S9
E	2017-07-11T22:33	22:35	1.37	1.46	S3 S9
F	2017-07-17T07:48	07:50	8.62	5.78	S8 S14
G	2017-07-26T00:02	00:00	1.44	1.24	F2 F3
H	2017-07-26T07:00	07:00	1.91	1.63	S4 S10
I	2017-07-26T07:27	07:25	5.18	0.39	S6 S12
J	2017-08-06T05:13	05:15	7.70	0.63	S6 S12
K	2017-08-07T15:37	15:35	3.22	1.57	S6 S12
L	2017-08-23T17:53	17:55	1.88	0.54	S4 S10
M	2018-08-15T11:57	11:55	1.47	0.70	F2 F3
N	2018-08-26T06:38	06:40	2.85	2.17	S6 S12
O	2018-08-27T11:39	11:40	0.95	1.65	S4 S10
P	2018-08-27T12:14	12:15	7.43	1.19	S7 S13
Q	2018-09-10T17:14	17:15	0.78	1.02	S4 S10
R	2018-09-10T23:57	23:55	0.88	1.64	S5 S11
S	2019-07-25T21:40	21:40	1.45	4.26	S5 S11
T	2019-08-31T12:01	12:00	1.88	0.68	S7 S13
U	2019-09-06T04:38	04:40	3.57	0.77	S7 S13
V	2020-08-02T16:58	17:00	1.06	0.61	S5 S11
W	2020-08-02T17:09	17:10	0.65	0.55	F2 F3
X	2020-08-03T01:04	01:05	1.03	2.11	S5 S11
Y	2020-08-05T14:19	14:20	1.13	3.94	F2 F3
Z	2020-08-29T09:56	09:55	3.26	1.73	S7 S13